

# Overcoming ammonia synthesis scaling relations with plasma-enabled catalysis

Prateek Mehta<sup>1</sup>, Patrick Barboun<sup>1</sup>, Francisco A. Herrera<sup>2</sup>, Jongsik Kim<sup>1</sup>, Paul Rumbach<sup>2</sup>, David B. Go<sup>1,2\*</sup>, Jason C. Hicks<sup>1\*</sup> and William F. Schneider<sup>1\*</sup>

**Correlations between the energies of elementary steps limit the rates of thermally catalysed reactions at surfaces. Here, we show how these limitations can be circumvented in ammonia synthesis by coupling catalysts to a non-thermal plasma. We postulate that plasma-induced vibrational excitations in N<sub>2</sub> decrease dissociation barriers without influencing subsequent reaction steps. We develop a density-functional-theory-based microkinetic model to incorporate this effect, and parameterize the model using N<sub>2</sub> vibrational excitations observed in a dielectric-barrier-discharge plasma. We predict plasma enhancement to be particularly great on metals that bind nitrogen too weakly to be active thermally. Ammonia synthesis rates observed in a dielectric-barrier-discharge plasma reactor are consistent with predicted enhancements and predicted changes in the optimal metal catalyst. The results provide guidance for optimizing catalysts for application with plasmas.**

The rates of heterogeneous catalytic processes are governed by the adsorption energies of reaction intermediates and activation energies along pathways that connect these intermediates. For a wide range of reactions on a variety of catalyst surfaces, it has been shown that the adsorption energies of various intermediates are correlated to one another by linear scaling relationships<sup>1</sup>. Furthermore, the activation energies are typically linearly related to adsorption energies through Brønsted–Evans–Polanyi relationships<sup>2,3</sup>. When they hold, these relationships significantly reduce the number of independent parameters available for tuning catalyst performance, often placing severe limitations on the maximum achievable activity or selectivity<sup>4,5</sup>.

A classic example of these correlation-imposed constraints is the ammonia synthesis reaction,  $\text{N}_2 + 3\text{H}_2 \rightleftharpoons 2\text{NH}_3$  (refs <sup>4,6</sup>). An ideal catalyst for this reaction should be able to stabilize the transition state for N<sub>2</sub> dissociation while simultaneously having a weak affinity for NH<sub>x</sub> ( $x=0, 1$  or  $2$ ) intermediates in order to not limit further reaction and/or desorption of NH<sub>3</sub>. However, because these activation and adsorption energies are correlated with each other on conventional metal catalysts, it is not possible to adjust these energies independently. As a consequence, optimization of these catalysts has been restricted along a volcano-type relation in a one-dimensional parameter space<sup>7,8</sup> and, even on the best identified materials, practical rates are only attainable at elevated temperatures ( $\sim 700$  K) and pressures ( $\sim 100$  atm). Finding ways to circumvent the scaling relations may provide a path towards enabling a more sustainable low-temperature and -pressure ammonia synthesis process<sup>4,6,9</sup>.

While ammonia synthesis catalysts that are not bound by scaling relations remain elusive, one way of overcoming the above limitations is to assist nitrogen dissociation by applying an external stimulus. For instance, promotion of N<sub>2</sub> into less stable vibrationally or electronically excited states may reduce the activation energy for N<sub>2</sub> dissociation without influencing subsequent reaction steps. Non-thermal plasmas, generated by weakly ionizing the source gas via an electric discharge, are rich sources of such vibrationally and electronically excited molecules, along with other reactive species such as radicals, ions and free electrons. Because these plasmas operate

far from thermal equilibrium, the activated species can be generated without significantly increasing bulk gas temperature. Several studies have now demonstrated that promising yields of ammonia can be obtained at low temperature (400–500 K) and atmospheric pressure when a non-thermal plasma is operated in tandem with a catalyst<sup>10–19</sup>. It has been suggested that a plasma-catalytic ammonia synthesis process relying on renewable electricity could be particularly suitable for small-scale production<sup>15,18</sup>; in fact, one such process has recently been patented<sup>20</sup>. While these reports are encouraging, it is unclear whether the low-temperature and -pressure activity in a plasma-enabled process can rival that of the conventional Haber–Bosch process (100–200 atm and 600–800 K). Very little is known about the fundamental mechanisms involved and the roles played by the activated species. As a result, optimization of plasma-catalyst systems has so far been limited to trial-and-error experimentation—commonly starting with the best-known thermal catalysts (or cheap alternatives) and studying the influence of operational parameters (for example, flow rates, reactant composition, reactor type, plasma power, and so on) on performance.

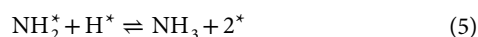
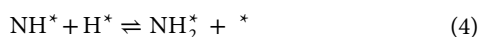
In this article, we report an analysis that shows that ammonia synthesis scaling relations can be overcome through vibrational excitation of N<sub>2</sub> in a plasma-enabled catalytic process. Vibrational excitations are a natural starting point for the development of concepts that link traditional thermochemical catalysis and plasma catalysis. Vibrational excitation has significantly lower excitation energy thresholds compared with other forms of excitation (for example, electronic excitation, ionization or dissociation) and is thus the predominant excitation channel for N<sub>2</sub> in non-thermal plasmas<sup>21</sup>. Furthermore, the rates of dissociation of impinging gas molecules are known to increase when they are vibrationally excited<sup>22–28</sup>. We first build a microkinetic model that combines density functional theory (DFT)-calculated energies of ammonia synthesis intermediates and information about nitrogen vibrational states extracted through experimental characterization of a dielectric-barrier-discharge (DBD) plasma. The model shows that the optimal catalysts and active sites in plasma catalysis may differ from those in thermal catalysis. Moreover, the low-temperature and -pressure

<sup>1</sup>Department of Chemical and Biomolecular Engineering, University of Notre Dame, Notre Dame, IN, USA. <sup>2</sup>Department of Aerospace and Mechanical Engineering, University of Notre Dame, Notre Dame, IN, USA. \*e-mail: [dgo@nd.edu](mailto:dgo@nd.edu); [jhicks3@nd.edu](mailto:jhicks3@nd.edu); [wschneider@nd.edu](mailto:wschneider@nd.edu)

ammonia synthesis rates on these optimal materials are predicted to be comparable to the high-temperature and -pressure Haber-Bosch rates. Experimental evaluations of  $\text{NH}_3$  synthesis rates at ambient pressure using a DBD plasma confirm that  $\text{NH}_3$  production is enhanced in the presence of supported metal catalysts; rates far exceed thermal rates at the same conditions; and relative trends in rate enhancement follow prediction. This work represents a first step towards the rational design of materials for plasma catalysis.

## Results

**Microkinetic modelling.** We begin with a discussion of the thermal ammonia synthesis reaction, which has been found to be well described by the following elementary steps<sup>8,29,30</sup>:



Here,  $^*$  represents a free surface site and  $\text{X}^*$  represents intermediate X adsorbed on a surface site. In this work, we calculated ammonia synthesis turnover frequencies (TOFs) employing a mean-field microkinetic model consisting of the same elementary steps, with DFT-calculated reaction and activation energies obtained from the literature<sup>8,31–33</sup>. We did not assume a priori that nitrogen dissociation was rate limiting, and we solved for steady-state coverages using a combination of ordinary differential equation integration and root-finding<sup>34</sup>.

Calculated rates for thermal ammonia synthesis at temperatures and pressures representative of Haber-Bosch conditions (673 K and 100 atm) and target<sup>9</sup> low-temperature and -pressure conditions (473 K and 1 atm) are compared in Fig. 1. Haber-Bosch rates are shown for step sites (which are generally considered to be the active sites), while rates at the target conditions are shown for both steps (orange) and terraces (green). Our results recover the volcano curve predicted by literature models<sup>7,8</sup> and indicate that Ru and Fe are the optimal monometallic catalysts at high temperature and pressure. At reduced temperature and pressure, rates on the same stepped surfaces are several orders of magnitude lower than the corresponding Haber-Bosch rates. Rates on terrace sites are a further few orders of magnitude lower. The results in Fig. 1 highlight the magnitude of rate improvements required of a plasma-assisted catalytic process to facilitate low-temperature and -pressure production.

We now elaborate the thermal microkinetic model to incorporate the influence of  $\text{N}_2$  vibrational excitation on surface reaction rates. A schematic representation of the promotion of  $\text{N}_2$  dissociation probability by vibrational excitation is shown in Fig. 2a. The potential energy diagram for dissociation of a ground state gas molecule with activation energy,  $E_a$  is shown in blue. In the vibrationally excited state, the energy of the initial state is increased by the energy of vibration,  $E_v$ . In the ideal case, this increase in initial state energy would lower the dissociation barrier by an equivalent  $E_v$  (green dashed curve). For the more general case in which the vibrational coordinate does not project directly onto the reaction coordinate<sup>28</sup>, the reduction in activation barrier can be written as  $E_v$  multiplied by an efficiency factor  $\alpha$  (orange curve). For  $\text{N}_2$ , which has a single, extended vibrational ladder and a relatively large vibrational spacing ( $\sim 0.3$  eV), significant enhancements in the dissociation rates may be possible through vibrational excitation.

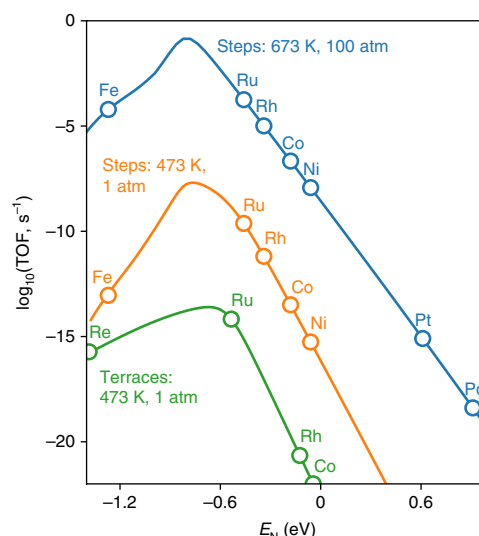


**Fig. 1 | Modelled ammonia synthesis rates during thermal catalysis.**

Rates on metal step sites under representative Haber-Bosch conditions are shown in blue. Rates under the less severe target conditions on metal steps and terraces are shown in orange and green, respectively. Reaction conditions:  $\text{N}_2:\text{H}_2 = 1:3$ ;  $\text{N}_2$  conversion = 1%.

For nitrogen molecules in the vibrational state  $v$ , we can now write the forward rate constant,  $k_v^{(f)}$ , of the reaction in equation (1) as<sup>21</sup>,

$$k_v^{(f)} = A \exp \left( -\frac{E_a^{(f)} - \alpha E_v}{k_B T} H(E_a^{(f)} - \alpha E_v) \right) \quad (6)$$

where  $A$  is the pre-exponential factor,  $T$  is the gas temperature,  $k_B$  is the Boltzmann constant and  $H(x)$  is the Heaviside step function,

$$H(x) = \begin{cases} 0, & x < 0 \\ 1, & x \geq 0 \end{cases} \quad (7)$$

We note that in the above expression the vibrational degree of freedom is not included in the pre-exponential factor; all other degrees of freedom are in thermal equilibrium<sup>35</sup>.

For homogeneous, gas-phase reactions,  $\alpha$  is often described using the Fridman-Macheret model<sup>21</sup>:

$$\alpha = \frac{E_a^{(f)}}{E_a^{(f)} + E_a^{(b)}} \quad (8)$$

Here,  $E_a^{(f)}$  and  $E_a^{(b)}$  are the activation barriers for the forward and backward reactions. This expression is motivated by molecular reaction dynamics theories proposed by Polanyi<sup>36</sup>, which state that translational energy contributes more significantly to overcoming the early transition states associated with exothermic reactions and that vibrational energy contributes more significantly to overcoming the late transition states associated with endothermic reactions. Polanyi's rules generally also apply for gas-surface reactions<sup>26,28,37</sup>, but an expression analogous to equation (8) has not been developed for such reactions. We adopt the Fridman  $\alpha$  model in equation (8) to modulate the effect of  $\text{N}_2$  vibrational excitation on surface dissociation rates. It should be noted that this choice of  $\alpha$  does not impact the qualitative trends predicted by our model, but absolute rate predictions are sensitive to this choice. The Fridman  $\alpha$  is plotted as a

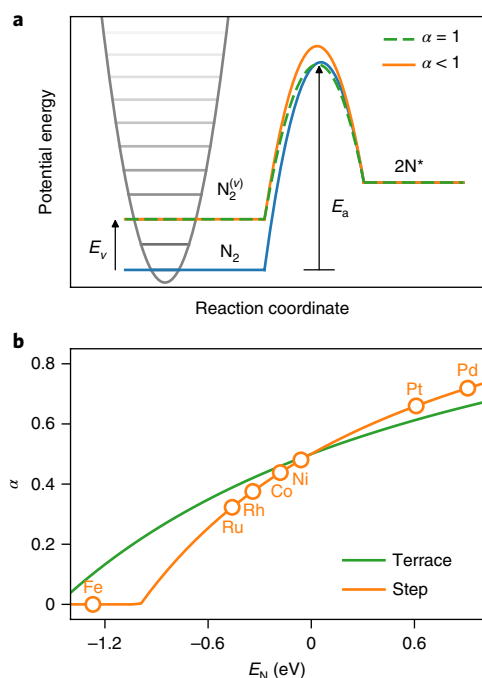


**Fig. 2 | Relationships between the  $N_2$  vibrational state and effective dissociation barrier.** **a**, Schematic reaction coordinate comparing activation energies for  $N_2$  dissociation starting from ground (blue) or second vibrationally excited states. The dashed green and orange curves correspond to a vibrational efficiency ( $\alpha$ ) of unity and less than unity, respectively. **b**, Variation of the Fridman  $\alpha$  factor as a function of nitrogen binding energy on steps and terraces.  $\alpha$  vanishes in the limit that dissociation is non-activated, as occurs at  $E_N < -1$  on steps.

function of the nitrogen binding energy on steps and terraces in Fig. 2. For metals that strongly bind nitrogen,  $E_a^{(f)}$  is low (the Brønsted–Evans–Polanyi relation), and thus  $\alpha$  is low. In contrast, on metals where nitrogen dissociation is endothermic,  $E_a^{(f)}$  and  $\alpha$  values are larger.

In a DBD plasma, inelastic collisions with electrons and vibrational–vibrational energy exchange excite  $N_2$  vibrational states to temperatures much greater than the bulk gas temperature<sup>21,38</sup>. Furthermore, these vibrational states are expected to follow non-Boltzmann statistics<sup>21,38</sup>. To gain information about this excitation, we performed optical emission spectroscopy (OES) measurements in a DBD reactor in the presence of a catalyst, as well as one without any packing. The spectra were obtained by integrating the optical emission over space and time. The spectra were then curve fit using Specair<sup>39</sup>, and the vibrational temperature of  $N_2$  ( $T_{\text{vib}}$ ) was extracted as a fitting parameter. For comparison, the bulk gas temperature ( $T_{\text{gas}}$ ), measured using an in situ thermocouple, was  $398.5 \pm 5$  K. Figure 3a shows the  $T_{\text{vib}}$  of  $N_2$  at different  $N_2:H_2$  ratios for the case when the reactor was packed with 100 mg of 5% Ni/ $Al_2O_3$  catalyst and operated under a 10 W DBD plasma. We found that the estimated  $N_2$  vibrational temperature had a weak dependence on the gas composition and that the catalyst and support had no appreciable impact on the plasma properties (see Supplementary Fig. 7). An average value of  $T_{\text{vib}} = 3,000$  K was used in our model.

Using the vibrational temperature, a simple estimate of the non-Boltzmann population densities of vibrationally excited  $N_2$  states in the plasma can be obtained using the Treanor formula<sup>21,40,41</sup>,

$$p_v(v, T_{\text{vib}}, T_{\text{gas}}) = B \exp \left( -\frac{\hbar \omega v}{T_{\text{vib}}} + \frac{x_e \hbar \omega v^2}{T_{\text{gas}}} \right) \quad (9)$$

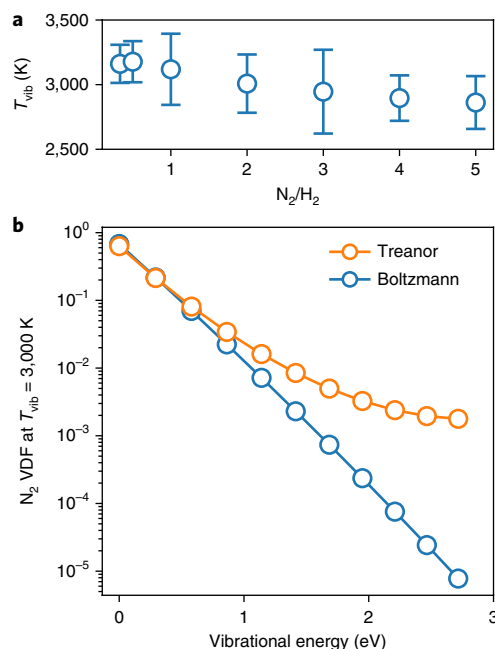


**Fig. 3 | Plasma-induced vibrational excitation of  $N_2$ .** **a**, Vibrational temperature of  $N_2$  versus the  $N_2:H_2$  ratio as determined by OES. The plasma power was 10 W and the reactor was packed with 100 mg 5% Ni/ $Al_2O_3$ . Error bars reflect uncertainty at 95% confidence. **b**, Treanor (orange) and Boltzmann (blue) vibrational distribution functions (VDFs) for  $N_2$  at  $T_{\text{vib}} = 3,000$  K and  $T_{\text{gas}} = 473$  K.

Here,  $B$  is a normalization constant,  $\hbar$  is the reduced Planck's constant,  $\omega$  is the vibrational frequency and  $x_e$  is the anharmonicity coefficient. By including the anharmonicity of the  $N_2$  molecules, the Treanor distribution captures the non-resonant vibrational–vibrational energy transfer mechanism that results in the overpopulation of higher-energy vibrational states. However, the Treanor formula does not capture the depopulation of highly excited vibrational states by vibration-to-translation relaxations or via direct dissociation in the plasma phase, resulting in an exponentially parabolic distribution. To account for the depopulation of highly excited levels, we truncate the distribution at the Treanor minimum (which includes the first 10 vibrationally excited states) to compute the normalized population densities. The normalized Treanor population densities at  $T_{\text{vib}} = 3,000$  K and  $T_{\text{gas}} = 473$  K are plotted in Fig. 3b. We find that the Treanor distribution predicts that only about 63.2% of  $N_2$  remains in the ground vibrational state. The first vibrationally excited state has a population of 21.4%, while the states in the tail of the distribution ( $v_8-v_{10}$ ) have probabilities of around 0.2%. For comparison, the equilibrium Boltzmann distribution at  $T_{\text{vib}} = 3,000$  K is plotted in blue in Fig. 3b. While the populations of the first few vibrational states are similar in both the Boltzmann and the Treanor distribution, the Boltzmann distribution does not consider vibrational–vibrational processes, and thus predicts populations of higher vibrational states that are orders of magnitude lower than the Treanor distribution.

We can now write reaction (1) as a collection of state-specific reactions of the form,  $N_2^{(v)} + 2^* \rightleftharpoons 2N^*$ , whose individual rates are given by,

$$r_1(v) = k_v^{(f)} p_v P_{N_2} \theta_s^2 - k_v^{(b)} \theta_N^2 \quad (10)$$

In the above equation,  $P_{N_2}$  is the partial pressure of  $N_2$ , and  $\theta_N$  and  $\theta_s$  are the coverages of adsorbed nitrogen and free sites, respectively. The forward rate constant,  $k_v^{(f)}$ , is computed using equation (6)

and the corresponding backward rate constant,  $k_v^{(b)}$ , is computed as  $k_v^{(b)} = k_v^{(f)} / K_v$ . Here,  $K_v$  is a vibrational state-specific equilibrium constant (where the non-equilibrium vibrational degree of freedom is treated explicitly). It should be noted that the reaction becomes more exothermic with increasing vibrational state (see Fig. 2a), and  $K_v$  increases accordingly. The probability weighted rate of the reaction shown in equation (1) is then simply  $\sum r_i(v)$ . While plasma excitation may also similarly influence  $H_2$  dissociation (equation (2)), we assume that this step remains fast compared with  $N_2$  dissociation. Furthermore, we assume that the hydrogenation steps are unaffected by the plasma. Thus, the rate expressions for the reactions in equations (2)–(5) in our plasma-catalysis model are identical to the corresponding expressions in thermal catalysis.

Using the modified rate expressions, the vibrational-distribution-weighted (plasma-on) reaction rates at the target conditions (473 K and 1 atm) were computed and compared with the thermal catalytic (plasma-off) rates from Fig. 1. This comparison is shown in Fig. 4 for step and terrace sites. For both types of site, the optimal plasma-on reaction rates (that is, the peaks of the volcano curves) are several orders of magnitude higher than those for thermal catalysis. For step sites (Fig. 4a), the peak of the plasma-on volcano curve shows a distinct shift towards weaker nitrogen binding energies, predicting Co and Ni to be near the volcano peak. Comparing the low-temperature and -pressure plasma-on volcano curve with the high-temperature and -pressure Haber–Bosch curve in Fig. 1, we find that rates on the optimal plasma-on catalyst are comparable to those on the optimal thermal catalyst at 673 K and 100 atm Ru steps.

The rightward shift of the plasma-on volcano peak for metal steps can be understood using a Sabatier analysis<sup>3</sup> for the hydrogenation reactions. These Sabatier rates, plotted as grey dashed lines, are the maximum rates possible (that is, under ideal coverages) for the  $NH_x$  ( $x=0, 1, 2$ ) hydrogenation steps (reactions in equations (3)–(5)):

$$R_{\text{Sab}} = \min\left(\frac{1}{2}r_3^{\text{max}}, \frac{1}{2}r_4^{\text{max}}, \frac{1}{2}r_5^{\text{max}}\right) \quad (11)$$

The maximum achievable rate through  $N_2$  vibrational excitation is bounded by the Sabatier lines for the hydrogenation steps; that is, rate enhancements by vibrational excitation are only possible as long as  $N_2$  dissociation is rate limiting. Metals that bind nitrogen less strongly have smaller hydrogenation barriers and consequently the rate enhancements are higher for these metals. Rate enhancements are minimal for metals on the left leg of the plasma-off volcano curve because the rate is limited by site poisoning rather than  $N_2$  activation. It should be noted that the exact extent to which the volcano peak is shifted towards the right is sensitive to the model choices, including the nature and truncation of the vibrational distribution, as well as the rate enhancement factor  $\alpha$ . This sensitivity also implies opportunities to further improve performance by tuning the plasma properties. For instance, higher ammonia synthesis rates may be obtained on metals on the right of Co or Ni if high-energy vibrational states could be populated more than is considered here.

For terrace sites (Fig. 4b), a similar shift of the plasma-on volcano peak is not observed, indicating that  $N_2$  dissociation remains the rate-limiting step. Indeed, the  $N_2$  activation energies on terrace sites are significantly higher than for steps (see Supplementary Figs. 1–4). Ru remains the most active metal terrace under plasma-on conditions, although the TOF on these sites are predicted to be two orders of magnitude lower than on Co steps. However, the plasma-on TOF on Ru terrace sites is of the same order of magnitude as that on Ru steps, despite the fact that their plasma-off TOFs are five orders of magnitude apart. This result suggests the possibility of a change of active site for ammonia synthesis from a step site to a terrace site if sufficient excitation of  $N_2$  can be achieved in the plasma phase. The Sabatier line in Fig. 4b lends further support

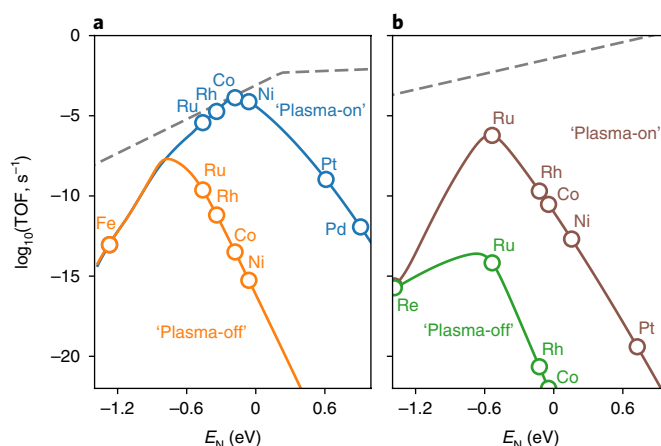


**Fig. 4 | Rate enhancements with plasma-induced  $N_2$  vibrational excitation.**

**a, b.** Comparison of  $N_2$  vibrational-distribution-weighted (plasma-on) and thermal (plasma-off) ammonia synthesis rates on step (**a**) and terrace (**b**) sites. Reaction conditions: 1 atm,  $T_{\text{gas}} = 473$  K,  $T_{\text{vib}} = 3,000$  K, conversion = 1%. The dashed lines are the maximum possible rates for the hydrogenation reactions.

to this idea—because the activation barriers for the hydrogenation reactions are lower on terraces, the upper bound for rate enhancements by vibrational excitation is higher.

While the above discussion is focused on the effects of vibrational excitation, the results also provide insights into how other forms of  $N_2$  excitations may influence the activity trends. We anticipate that electronic excitation, ionization and dissociation will also reduce (or eliminate) the activation barrier for  $N_2$  dissociation and, like vibrational excitation, will shift the active sites for ammonia synthesis to more noble ones.

**Plasma-catalytic kinetics.** We measured  $NH_3$  synthesis rates on a series of catalysts selected to span the top of the predicted volcano curves. We compared five different metal catalysts (Fe, Ru, Co, Ni and Pt) supported on  $\gamma$ -alumina (100 g of material, 5 wt.% metal). Experiments were performed in a DBD plasma reactor similar to the one used in our previous studies of methane dry reforming<sup>42,43</sup>. The DBD plasma was operated at 10 W and ~20 kHz at atmospheric pressure, and the reactor temperature was maintained at 438 K. The catalysts were verified as thermally inactive under these conditions. As expected based on literature reports<sup>10–12,14,15</sup>, some  $NH_3$  was produced when  $N_2$  and  $H_2$  were passed through the plasma alone (empty DBD reactor) or when they were flowed through the reactor packed with  $\gamma$ - $Al_2O_3$ . Ammonia yields were found to increase with the introduction of the metal catalysts, most substantially for the Ni and Co catalysts. In a series of test experiments with varying  $N_2:H_2$  feed compositions, it was found that non-stoichiometric ratios in the range of 1:1 to 3:1 produced higher ammonia yields than the stoichiometric 1:3 ratio, similar to previous reports<sup>12,14</sup> (see Supplementary Fig. 10). Accordingly, to compare the performance of different catalysts, we used an  $N_2:H_2$  ratio of 2:1.

To make a connection to model predictions, ammonia synthesis rates on the various catalysts were measured under the above conditions as a function of residence time, defined as the mass of material divided by the mass-flow rate of the reactants ( $W/F$ ) (plotted in Supplementary Fig. 11). Rates as a function of  $W/F$  were also measured to elucidate background contributions (that is, the reactor packed with 100 mg of the  $\gamma$ -alumina support). To ensure that comparisons were made in the kinetic regime, rates were extrapolated to initial rates ( $r^0$ ) in the limit of zero residence time; that is,  $W/F=0$  (see Supplementary Methods). From the initial



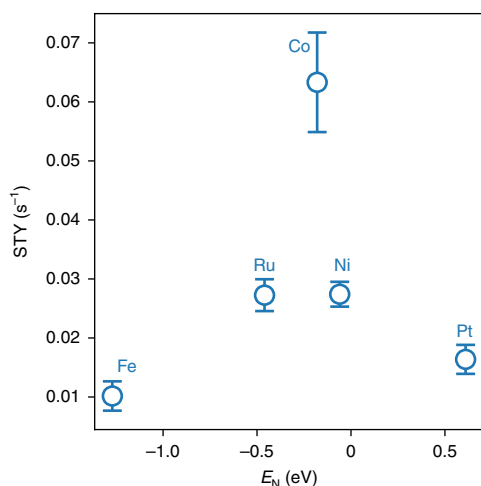


**Fig. 5 | Experimental plasma-catalytic kinetics.** Measured ammonia STYs in the DBD reactor on metal/ $\text{Al}_2\text{O}_3$  catalysts as a function of the DFT-calculated nitrogen adsorption energy. Reaction conditions:  $\text{N}_2:\text{H}_2 = 2:1$ , total pressure = 1 atm, plasma power = 10 W, reactor temperature = 438 K. Error bars indicate the s.d. in the STY.

rates, the reactivity of the catalysts was compared by calculating the site-time yield (STY) of ammonia:

$$\text{STY} = \frac{r_{\text{M}/\text{Al}_2\text{O}_3+\text{DBD}}^0 - r_{\text{Al}_2\text{O}_3+\text{DBD}}^0}{n_{\text{sites}}} \quad (12)$$

We subtracted the initial rates of the background reaction to ensure that only rate contributions intrinsic to the metal were compared.  $n_{\text{sites}}$  in equation (12) are the moles of catalytically active sites per gram of material. Because both steps and terrace sites may potentially be active in plasma catalysis for some of the tested materials (as predicted by Fig. 4), we estimated  $n_{\text{sites}}$  using CO chemisorption, which probes both steps and terraces. The STY estimates are thus expected to be a lower limit, especially for metals on the right of the volcano curve for which the activity of step sites dominates. Measured STYs are plotted against the DFT-calculated nitrogen adsorption energy in Fig. 5. A clear variation in activity versus metal catalyst is evident, and the observed activity trend of  $\text{Co} > \text{Ni} = \text{Ru} > \text{Pt} > \text{Fe}$  tracks remarkably well with model predictions. We note that absolute correspondence between the measured STY and modelled TOF should not be expected given the simplicity of the model and differences in site normalization between the model and experiments. However, the measured STY provides strong evidence both of a plasma-catalyst interaction that enhances  $\text{NH}_3$  synthesis rates well over thermal rates under the same conditions and a shift in the volcano maximum to weaker binding metals, consistent with model predictions.

## Conclusions

Application of a non-thermal plasma to a catalytic system can selectively activate certain degrees of freedom of gas molecules, allowing manipulation of reaction energetics in a way that is not possible in conventional thermal catalysis. Using a microkinetic model that incorporates nitrogen vibrational excitations expected of a non-thermal  $\text{N}_2:\text{H}_2$  plasma, we predict that it is possible to produce  $\text{NH}_3$  at low temperatures and atmospheric pressure in plasma-catalytic reaction environments at rates that can match those of the high-temperature and -pressure Haber–Bosch process. However, such rates cannot be achieved on catalyst motifs that are most active for thermal catalysis; instead, the optimal catalyst is shifted to sites that

bind nitrogen more weakly. The shift in optimal catalyst is confirmed by kinetic experiments in a plasma reactor, showing that the idealized model can provide the essential insights to help guide the design of plasma-catalytic systems. The work thus represents an important step forwards in connecting plasma catalysis to well-established concepts of conventional heterogeneous catalysis.

Our analysis also highlights opportunities for further improvements in reaction rates through careful control of the plasma properties. For example, populations of high-energy excited states could be increased using high-voltage pulsed discharges<sup>14,44</sup>. Another possibility is the use of warm plasmas, such as microwave<sup>45</sup> or gliding arc discharges<sup>46</sup>, which are known to be more effective in populating high-energy vibrational states than the DBD discharge discussed here, albeit at higher gas temperatures. Post-plasma catalysis may be an option for these higher-temperature plasmas. With sufficient excitation of high-energy states, active sites for ammonia synthesis may transition from step sites to terrace sites, enabling more atom-efficient catalysis.

## Methods

**Computational details.** Adsorption and activation energies for the ammonia synthesis intermediates were collected from the literature<sup>8,31,33</sup>. Most of these energies are also tabulated in the CatApp database<sup>32</sup>. In these reports, all calculations were performed using the DACAPO code, with exchange and correlation effects described by the RPBE functional<sup>47</sup>. Core electrons were described using Vanderbilt ultrasoft pseudopotentials. The plane-wave cutoff used was at least 340 eV. Further details of the calculations can be found in the respective papers. The energies were verified for consistency and it was found that the same overall reaction energies were produced for steps and terrace sites. The adsorption energy of nitrogen,  $E_{\text{N}}$ , was used as a descriptor for the microkinetic models, and the energies of all other intermediates and transition states were obtained through scaling relations or Brønsted–Evans–Polanyi relationships (plotted in Supplementary Figs. 1–4). Standard entropies for gas-phase species were obtained from the National Institute of Standards and Technology (NIST) Chemistry WebBook (<http://webbook.nist.gov/chemistry>). Surface-bound species were treated in the frozen adsorbate limit. Zero-point energies for the gas species were calculated from vibrational frequencies obtained from the NIST Computational Chemistry Comparison and Benchmark Database<sup>48</sup>. For the adsorbed species, vibrational frequencies on Ru(211) were used to calculate the zero-point energies. These vibrational frequencies were taken from ref. <sup>8</sup> (for nitrogen-containing intermediates) and ref. <sup>30</sup> (for hydrogen). Coverage effects on the adsorption energies and entropies were not included during construction of the volcano curves, similar to previous reports on thermal ammonia synthesis<sup>3,7,8</sup>. This neglect of coverage effects is not expected to strongly influence the relative ordering of the metals or the position of the volcano peak. However, we note that the absolute rates of metals on the far left of the volcano curve (that is, those that bind adsorbates very strongly) are known to be significantly underestimated for some reactions when coverage effects are not included<sup>49,50</sup>. All steps were considered to be potentially rate limiting. Steady-state coverages of the reaction intermediates were first pre-converged through integration of the coupled ordinary differential equations, and subsequently refined using an arbitrary precision root-finding algorithm<sup>34</sup>. Overall reaction rates were obtained from the steady-state surface coverages. The spectroscopic constants for modelling the vibrational levels of  $\text{N}_2$  were taken from ref. <sup>51</sup>. The code required to solve the microkinetic models is provided as a python module in the supporting information, along with examples of reproducing the results of this study.

**Plasma characterization.** OES was performed on a modified, L-shaped quartz reactor tube (shown in Supplementary Fig. 5) consisting of an 8-mm-diameter tube with a 5 mm inner diameter bent at a 90° angle. The catalyst material was packed into the 90° bend where a planar quartz window was integrated into the tube to allow for emission measurements. This configuration allowed for more effective optical access to the catalyst-packed bed than the straight reactor tube configuration used for ammonia synthesis kinetic measurements; OES measurements conducted on both configurations confirmed that the geometry did not appreciably alter the quantitative data. To generate the DBD plasma, a tungsten electrode was inserted into the reactor tube and a 6-cm-long stainless steel mesh electrode was attached to the outside. The current  $i_t$  and voltage  $V_t$  were measured during all experiments. The current was obtained by measuring the voltage drop across a test resistor ( $R = 100 \Omega$ ) placed in series with the plasma. The average plasma power was found by averaging the instantaneous power ( $P_t = V_t i_t - i_t^2 R$ ) over one cycle. The DBD plasma was driven by an AC power supply (PVM500) using a sinusoidal waveform at ~20 kHz; the plasma power was maintained at 10 W for all measurements. An optical fibre connected to an Ocean Optics USB2000+ spectrometer recorded emission data. In the configuration with no catalyst, an

integration time of 0.01 s was employed, while in the configurations with either a 100 mg  $\text{Al}_2\text{O}_3$  support or a 100 mg  $\text{Al}_2\text{O}_3$  support mixed with 5% Ni catalyst, an integration time of 0.05 s was used. Measurements were conducted in pure  $\text{N}_2$  and  $\text{H}_2$  at a fixed total flow rate of 20 standard cubic centimetres per minute with the flow ratio of  $\text{N}_2/\text{H}_2$  varying from 0.33 to 5.0. For all ratios, the experiments were conducted three times under both the no-catalyst condition and with the  $\text{Al}_2\text{O}_3$  support only, while the 5% Ni/ $\text{Al}_2\text{O}_3$  system was tested four times.

The second positive system of  $\text{N}_2$ , which produces emission lines from approximately 300–385 nm, was used to monitor the plasma<sup>52,53</sup>. The emission spectra (shown in Supplementary Fig. 6a) were curve fit using the commercial software Specair, which calculates the OES by determining the population of the upper state of the transitions based on a Boltzmann distribution and the specified temperatures of the internal energy modes<sup>54</sup>. The fitting parameters of the model are the electronic ( $T_{\text{elec}}$ ), vibrational ( $T_{\text{vib}}$ ) and rotational ( $T_{\text{rot}}$ ) temperatures of  $\text{N}_2$  (where it is assumed that the rotational and translational temperatures are approximately equal due to the fast relaxation time of the rotational states<sup>55–56</sup>) and the relative population of different atomic and molecular species within the mixture. The slit function, which is the representation of the instrument response and an input data of the software, was measured using a diode laser (Thorlabs) at 635 nm with the spectrometer. A theoretical spectrum was produced by convolving the theoretical emission spectrum with the slit function. In the range of 300–385 nm, the relative intensities of rotational–vibrational lines are independent of  $T_{\text{elec}}$ <sup>56</sup>, and thus only  $T_{\text{vib}}$  and  $T_{\text{rot}}$  were used as fitting parameters (see Supplementary Fig. 6b).

**Experimental kinetics.** Kinetic experiments were performed in a DBD reactor similar to the one used in our previous work<sup>42,43</sup>. The reactor consists of a quartz tube (7 mm outer diameter, 5 mm inner diameter) with a tungsten rod (1.5 mm diameter) inserted through the centre serving as the ground electrode. An external 6 cm length of stainless steel mesh (McMaster 200 × 1400 mesh) wrapped around the tube served as the high-voltage electrode. This configuration yields a discharge gap of 1.75 mm and a discharge volume of ~0.18 ml. Kinetic measurements were performed using five commercially available catalysts (Fe, Ru, Co, Ni and Pt from Riogen) supported on  $\gamma$ -alumina with a metal loading of 5 wt.%. Background measurements were conducted using  $\gamma$ -alumina (>97; Strem Chemicals) only. A Quantachrome Nova 2200e  $\text{N}_2$  physisorption instrument was used to determine the surface area of each of the catalysts. The number of active metal sites was determined through CO pulse chemisorption using a Micromeritics ChemiSorb 2750 instrument. Metal particle sizes were determined from transmission electron microscope images taken using an FEI Titan microscope. Average metal particle sizes are based on at least 300 particles. Catalyst characterization is further discussed in the Supplementary Methods. All characterization data are provided in Supplementary Table 1. X-ray diffraction patterns and transmission electron microscope images for the different catalysts are shown in Supplementary Figs. 8 and 9, respectively.

For each experiment, 100 mg of material was packed into the discharge region of the plasma reactor and held in place by a silica frit. Before measurement, the catalysts were pre-treated in hydrogen at 773 K for 30 min to remove any oxide layers that may have formed on the metal surface when exposed to the ambient environment. The DBD plasma was generated within the discharge region using a high-voltage AC power supply (PVM500) using a sinusoidal waveform at ~20 kHz. A power deposition of 10 W was maintained during all experiments and was monitored using an oscilloscope (Tektronix TDS3012B). The reactor temperature was maintained at 438 K for all measurements. The temperature was monitored with a thermocouple placed downstream from the discharge region immediately following the silica frit. Nitrogen (Airgas 99.98%) and hydrogen (Airgas 99.99%) were introduced into the system and controlled independently with mass-flow controllers (GFC17). The total gas flow rates were varied between 10 and 100 ml min<sup>-1</sup>, and the inlet reactant composition,  $\text{N}_2/\text{H}_2$ , was varied between 1/3 and 5. Ammonia production rates were monitored with an in-line gas chromatograph (7820A; Agilent Technologies) with a thermal conductivity detector using an Agilent CP-Volamine column. To quantify ammonia production, an external calibration was performed with a commercially mixed 10%  $\text{NH}_3/\text{He}$  gas cylinder. For all reactions, ammonia was the only product observed (that is, no hydrazine or other nitrogen-containing products were present). Reaction progress was monitored in terms of ammonia production due to the overlap of the hydrogen and nitrogen peaks in the gas chromatograph trace.

**Code availability.** Code can be found in the external Zenodo repository (<https://doi.org/10.5281/zenodo.1067912>). The microkinetic model is included as a python module (mkm.py). Other utility functions are included in plasmautils.py. Python scripts showing how these data files were used to create all the figures in the paper are provided in the Supplementary Data file.

**Data availability.** The Zenodo repository also hosts the raw data (<https://doi.org/10.5281/zenodo.1067912>). Data for the plasma characterization and kinetic measurements are included as Excel spreadsheets (Raw\_data\_OES.xlsx and kinetic-expts.xlsx). Calculated turnover frequencies are included as json files.

Received: 5 December 2017; Accepted: 21 February 2018;

Published online: 02 April 2018

## References

- Abild-Pedersen, F. et al. Scaling properties of adsorption energies for hydrogen-containing molecules on transition-metal surfaces. *Phys. Rev. Lett.* **99**, 016105 (2007).
- Evans, M. G. & Polanyi, M. Inertia and driving force of chemical reactions. *Trans. Faraday Soc.* **34**, 11–24 (1938).
- Bligaard, T. et al. The Brønsted–Evans–Polanyi relation and the volcano curve in heterogeneous catalysis. *J. Catal.* **224**, 206–217 (2004).
- Vojvodic, A. & Norskov, J. K. New design paradigm for heterogeneous catalysts. *Natl Sci. Rev.* **2**, 140–149 (2015).
- Greeley, J. Theoretical heterogeneous catalysis: scaling relationships and computational catalyst design. *Annu. Rev. Chem. Biomol. Eng.* **7**, 605–635 (2016).
- Medford, A. J. et al. From the Sabatier principle to a predictive theory of transition-metal heterogeneous catalysis. *J. Catal.* **328**, 36–42 (2015).
- Logadottir, A. et al. The Brønsted–Evans–Polanyi relation and the volcano plot for ammonia synthesis over transition metal catalysts. *J. Catal.* **197**, 229–231 (2001).
- Vojvodic, A. et al. Exploring the limits: a low-pressure, low-temperature Haber–Bosch process. *Chem. Phys. Lett.* **598**, 108–112 (2014).
- Norskov, J., Chen, J., Miranda, R., Fitzsimmons, T. & Stack, R. *Sustainable Ammonia Synthesis—Exploring the Scientific Challenges Associated with Discovering Alternative, Sustainable Processes for Ammonia Production* (US Department of Energy Office of Science, 2016).
- Bai, M., Zhang, Z., Bai, X., Bai, M. & Ning, W. Plasma synthesis of ammonia with a microgap dielectric barrier discharge at ambient pressure. *IEEE Trans. Plasma Sci.* **31**, 1285–1291 (2003).
- Mizushima, T., Matsumoto, K., Sugoh, J., Ohkita, H. & Kakuta, N. Tubular membrane-like catalyst for reactor with dielectric-barrier-discharge plasma and its performance in ammonia synthesis. *Appl. Catal. A* **265**, 53–59 (2004).
- Mizushima, T., Matsumoto, K., Ohkita, H. & Kakuta, N. Catalytic effects of metal-loaded membrane-like alumina tubes on ammonia synthesis in atmospheric pressure plasma by dielectric barrier discharge. *Plasma Chem. Plasma Process.* **27**, 1–11 (2006).
- Gómez-Ramírez, A., Cotrino, J., Lambert, R. M. & González-Elipe, A. R. Efficient synthesis of ammonia from  $\text{N}_2$  and  $\text{H}_2$  alone in a ferroelectric packed-bed DBD reactor. *Plasma Sources Sci. Technol.* **24**, 065011 (2015).
- Kim, H.-H., Teramoto, Y., Ogata, A., Takagi, H. & Nanba, T. Atmospheric-pressure nonthermal plasma synthesis of ammonia over ruthenium catalysts. *Plasma Process. Polym.* **14**, 1600157 (2016).
- Peng, P. et al. Atmospheric pressure ammonia synthesis using non-thermal plasma assisted catalysis. *Plasma Chem. Plasma Process.* **36**, 1201–1210 (2016).
- Xie, D. et al. Ammonia synthesis and by-product formation from  $\text{H}_2\text{O}$ ,  $\text{H}_2$  and  $\text{N}_2$  by dielectric barrier discharge combined with an Ru/ $\text{Al}_2\text{O}_3$  catalyst. *RSC Adv.* **6**, 105338–105346 (2016).
- Hong, J. et al. Plasma catalytic synthesis of ammonia using functionalized-carbon coatings in an atmospheric-pressure non-equilibrium discharge. *Plasma Chem. Plasma Process.* **36**, 917–940 (2016).
- Akay, G. & Zhang, K. Process intensification in ammonia synthesis using novel coassembled supported microporous catalysts promoted by nonthermal plasma. *Ind. Eng. Chem. Res.* **56**, 457–468 (2017).
- Iwamoto, M., Akiyama, M., Aihara, K. & Deguchi, T. Ammonia synthesis on wool-like Au, Pt, Pd, Ag, or Cu electrode catalysts in nonthermal atmospheric-pressure plasma of  $\text{N}_2$  and  $\text{H}_2$ . *ACS Catal.* **7**, 6924–6929 (2017).
- Akay, G. Ammonia production by integrated intensified processes. US Patent 20130309161A1 (2011).
- Fridman, A. *Plasma Chemistry*. (Cambridge Univ. Press, New York, NY, 2008).
- Rettner, C. T. & Stein, H. Effect of vibrational energy on the dissociative chemisorption of  $\text{N}_2$  on Fe(111). *J. Chem. Phys.* **87**, 770–771 (1987).
- Holmblad, P. M., Wambach, J. & Chorkendorff, I. Molecular beam study of dissociative sticking of methane on Ni(100). *J. Chem. Phys.* **102**, 8255–8263 (1995).
- Romm, L., Katz, G., Kosloff, R. & Asscher, M. Dissociative chemisorption of  $\text{N}_2$  on Ru(001) enhanced by vibrational and kinetic energy: molecular beam experiments and quantum mechanical calculations. *J. Phys. Chem. B* **101**, 2213–2217 (1997).
- Murphy, M. J., Skelly, J. F., Hodgson, A. & Hammer, B. Inverted vibrational distributions from  $\text{N}_2$  recombination at Ru(001): evidence for a metastable molecular chemisorption well. *J. Chem. Phys.* **110**, 6954–6962 (1999).
- Luntz, A. C. A simple model for associative desorption and dissociative chemisorption. *J. Chem. Phys.* **113**, 6901–6905 (2000).
- Diekhöner, L. et al.  $\text{N}_2$  dissociative adsorption on Ru(0001): the role of energy loss. *J. Chem. Phys.* **115**, 9028–9035 (2001).
- Smith, R. R. Preference for vibrational over translational energy in a gas-surface reaction. *Science* **304**, 992–995 (2004).

29. Ertl, G. in *Elementary Steps in Ammonia Synthesis* 109–132 (Springer, Boston, MA, 1991).
30. Honkala, K. Ammonia synthesis from first-principles calculations. *Science* **307**, 555–558 (2005).
31. Wang, S. et al. Universal transition state scaling relations for (de) hydrogenation over transition metals. *Phys. Chem. Chem. Phys.* **13**, 20760 (2011).
32. Hummelshøj, J. S., Abild-Pedersen, F., Studt, F., Bligaard, T. & Nørskov, J. K. CatApp: a web application for surface chemistry and heterogeneous catalysis. *Angew. Chem. Int. Ed.* **124**, 278–280 (2011).
33. Falsig, H. et al. On the structure sensitivity of direct NO decomposition over low-index transition metal facets. *Top. Catal.* **57**, 80–88 (2013).
34. Grabow, L. C. in *Computational Catalysis* 1–58 (Royal Society of Chemistry, Cambridge, 2013).
35. Hansen, F. Y., Henriksen, N. E., Billing, G. D. & Guldberg, A. Catalytic synthesis of ammonia using vibrationally excited nitrogen molecules: theoretical calculation of equilibrium and rate constants. *Surf. Sci.* **264**, 225–234 (1992).
36. Polanyi, J. C. Concepts in reaction dynamics. *Acc. Chem. Res.* **5**, 161–168 (1972).
37. Diaz, C. & Olsen, R. A. A note on the vibrational efficacy in molecule-surface reactions. *J. Chem. Phys.* **130**, 094706 (2009).
38. Cacciatore, M., Capitelli, M., De Benedictis, S., Dilonardo, M. & Gorse, C. in *Nonequilibrium Vibrational Kinetics* 5–46 (Springer, Berlin and Heidelberg, 1986).
39. Laux, C. O., Spence, T. G., Kruger, C. H. & Zare, R. N. Optical diagnostics of atmospheric pressure air plasmas. *Plasma Sources Sci. Technol.* **12**, 125–138 (2003).
40. Treanor, C. E., Rich, J. W. & Rehm, R. G. Vibrational relaxation of anharmonic oscillators with exchange-dominated collisions. *J. Chem. Phys.* **48**, 1798–1807 (1968).
41. Gordiets, B. F. & Zhdanok, S. in *Nonequilibrium Vibrational Kinetics* 47–84 (Springer, Berlin and Heidelberg, 1986).
42. Kim, J., Go, D. B. & Hicks, J. C. Synergistic effects of plasma–catalyst interactions for CH<sub>4</sub> activation. *Phys. Chem. Chem. Phys.* **19**, 13010–13021 (2017).
43. Kim, J., Abbott, M. S., Go, D. B. & Hicks, J. C. Enhancing C–H bond activation of methane via temperature-controlled, catalyst–plasma interactions. *ACS Energy Lett.* **1**, 94–99 (2016).
44. Neyts, E. C., Ostrikov, K. K., Sunkara, M. K. & Bogaerts, A. Plasma catalysis: synergistic effects at the nanoscale. *Chem. Rev.* **115**, 13408–13446 (2015).
45. Snoeckx, R. & Bogaerts, A. Plasma technology—a novel solution for CO<sub>2</sub> conversion? *Chem. Soc. Rev.* **46**, 5805–5863 (2017).
46. Wang, W., Patil, B., Heijkers, S., Hessel, V. & Bogaerts, A. Nitrogen fixation by gliding arc plasma: better insight by chemical kinetics modelling. *ChemSusChem* **10**, 2145–2157 (2017).
47. Hammer, B., Hansen, L. B. & Nørskov, J. K. Improved adsorption energetics within density-functional theory using revised Perdew–Burke–Ernzerhof functionals. *Phys. Rev. B* **59**, 7413–7421 (1999).
48. Johnson III, R. D. *NIST 101. Computational Chemistry Comparison and Benchmark Database* (National Institute of Standards and Technology, 1999).
49. Lausche, A. C. et al. On the effect of coverage-dependent adsorbate–adsorbate interactions for CO methanation on transition metal surfaces. *J. Catal.* **307**, 275–282 (2013).
50. Frey, K., Schmidt, D. J., Wolvertson, C. & Schneider, W. F. Implications of coverage-dependent O adsorption for catalytic NO oxidation on the late transition metals. *Catal. Sci. Technol.* **4**, 4356–4365 (2014).
51. Heijkers, S. et al. CO<sub>2</sub> conversion in a microwave plasma reactor in the presence of N<sub>2</sub>: elucidating the role of vibrational levels. *J. Phys. Chem. C* **119**, 12815–12828 (2015).
52. Li, S., Ma, C., Zhang, Q., Ren, C. & Lu, W. Ion nitriding of pure iron using high-density plasma beam generated by a tubular plasma source. *Surf. Coat. Technol.* **309**, 47–53 (2017).
53. Staack, D., Farouk, B., Gutsol, A. & Fridman, A. Characterization of a DC atmospheric pressure normal glow discharge. *Plasma Sources Sci. Technol.* **14**, 700–711 (2005).
54. Staack, D., Farouk, B., Gutsol, A. F. & Fridman, A. A. Spectroscopic studies and rotational and vibrational temperature measurements of atmospheric pressure normal glow plasma discharges in air. *Plasma Sources Sci. Technol.* **15**, 818–827 (2006).
55. Laux, C. in *Physico-Chemical Modeling of High Enthalpy and Plasma Flows* 1–55 (von Karman Institute Lecture Series 2002-07, Rhode-Saint-Genèse, 2002).
56. Hummelt, J. S., Shapiro, M. A. & Temkin, R. J. Spectroscopic temperature measurements of air breakdown plasma using a 110 GHz megawatt gyrotron beam. *Phys. Plasmas* **19**, 123509 (2012).

### Acknowledgements

This work was supported by the US Department of Energy, Office of Science, Basic Energy Sciences, Sustainable Ammonia Synthesis Program, under award number DE-SC-0016543. W.F.S. acknowledges additional support under award number DE-FG02-06ER15839. Computational resources were provided by the Notre Dame Center for Research Computing. We thank the Notre Dame Energy Materials Characterization Facility and Notre Dame Integrated Imaging Facility for use of the X-ray diffractometer and transmission electron microscope, respectively. P.M. acknowledges support through the Eilers Graduate Fellowship for Energy Related Research.

### Author contributions

P.M. developed the microkinetic model. P.B. and J.K. performed the ammonia synthesis rate experiments. F.A.H. and P.R. performed the plasma characterization. P.M., P.B., F.A.H., D.B.G., J.C.H. and W.F.S. co-wrote the manuscript.

### Competing interests

The authors declare no competing interests.

### Additional information

**Supplementary information** is available for this paper at <https://doi.org/10.1038/s41929-018-0045-1>.

**Reprints and permissions information** is available at [www.nature.com/reprints](http://www.nature.com/reprints).

**Correspondence and requests for materials** should be addressed to D.B.G. or J.C.H. or W.F.S.

**Publisher's note:** Springer Nature remains neutral with regard to jurisdictional claims in published maps and institutional affiliations.